Electron microscopy observation of electric field assisted sintering of stainless steel nanoparticles

Fei Wang¹, Qin Zhou^{1,*}, Xing-Zhong Li², Yongchul Yoo¹, Michael Nastasi³, Bai Cui^{1,2,*}

¹ Department of Mechanical & Materials Engineering, University of Nebraska–Lincoln, Lincoln, NE 68588, USA

² Nebraska Center for Materials and Nanoscience, University of Nebraska–Lincoln, Lincoln, NE, 68588, USA

³ Department of Nuclear Engineering, Texas A&M University, College Station, TX 77843, USA

Abstract

The intrinsic role of electrical current on the electric field assisted sintering (EFAS) process of stainless steel 316L nanoparticles has been revealed by both *ex situ* and *in situ* experiments. A novel device on the Si chip that has been designed and fabricated to fit into the sample holder of a transmission electron microscope for these experiments. The evolution of nanoparticle morphology and microstructures during the EFAS process has been studied using scanning electron microscopy (SEM) and transmission electron microscopy (TEM), which has been combined with the

^{*}Co-corresponding authors

simultaneous measurement of the electric voltage and current changes. A preliminary four-stage mechanism for the EFAS process of stainless steel 316L nanoparticles has been proposed based on these experimental investigations.

Keywords: electric field assisted sintering, stainless steel nanoparticles, *in situ* transmission electron microscopy

1. Introduction

Sintering is a critical process for the advanced manufacturing of alloys and ceramics below the melting temperature [1]. Sintering of crystalline materials occurs by vapor transport, surface diffusion, lattice diffusion, grain boundary diffusion, and plastic flow [2, 3]. Among these mechanisms, grain boundary diffusion is an important densification mechanism, which transports matter from grain boundaries into the pores between powders, in which the driving force is the reduction of overall free energy by the decrease of specific surface and interface areas [4]. The traditional sintering methods include pressureless sintering and pressure-assisted techniques such as hot uniaxial [5] or isostatic processing [6]. Over the last 30 years, field-assisted sintering techniques have been developed that use electrical or electromagnetic fields to enhance the sintering rate [7]. Electric field assisted sintering (EFAS) is a novel

sintering technique that has drawn strong interests from the manufacturing industries [8–10]. EFAS is the foundation process for a commercial technique, spark plasma sintering (SPS) [11] or pulse electric current sintering (PECS) [12], in which both a pulsed electrical current and a uniaxial pressure are applied for rapid sintering of metal [13] or ceramic powders [14–16].

In the EFAS process, an electrical current is passed through metal or ceramic powders. The powders are heated by Joule heating from the electrical current passing through them, which is more efficient than the conventional sintering processes in which the sample surface is heated by radiation from an enclosing furnace. The main features of the EFAS are the direct heating of material powders by an electric current and a high heating rate (up to 1000 °C/min) [17, 18]. The PECS process is capable of rapidly producing fully dense materials at lower temperatures for shorter times than the conventional pressureless sintering and hot pressing processes [19]. With those advantages, EFAS and PECS can produce dense material components with small grain size [20] and improved mechanical property [21], corrosion resistance [22], or optical transparency [23].

Despite the wide applications and advantages, the fundamental mechanisms involved during the EFAS process remain relatively unclear [24]. The intrinsic role of electrical current on the EFAS process is beyond the Joule heating from an electric current passing through the powders. Several possible mechanisms have been suggested, including plasma generation [25], electromigration [26], temperature gradient-driven

atom flux [27], electric field-induced Frenkel pair formation [18], and dielectric breakdown of the surface oxide film [28]. The early studies proposed that the electrical current can generate spark discharge and plasma through the ionization of gas between the powder particles, which can promote the elimination of absorbed gases and oxide layers on the surface of particles and activate the sintering process [29, 30]. However, this plasma generation theory has been questioned for lack of unambiguous experimental evidence [31]. For example, the experiments indicated that there is no plasma, sparking, or arcing present during the EFAS process [31]. A variety of recent research has been conducted on studying the effect of electric current on the sintering of metal particles. The insulating surface oxide films present on the surface of metal powders can affect the kinetics of neck formation and growth during the initial stage of sintering. The study of Chaim [32] suggested that the enhanced surface conductivity with rising temperature promotes electric field intensification at the inter-particle contact areas, which can lead to electric field induced dielectric breakdown of surface oxide films. Bonifacio et al., [33] provide experimental evidence for the dielectric breakdown of NiO film on Ni nanoparticles by in situ TEM observations with the application of electrical current to the particles. Stepwise current increments were found to be associated with the dielectric breakdown of NiO films at inter-powder contact areas. Groza et al., [34] reported that the dielectric breakdown of the oxide film around the contact region of tungsten particles could result in a "cleaned" surface on tungsten particles.

In conductive materials such as metals, the intrinsic role of electrical current on mass transport has also been demonstrated. The enhanced mass transport may be attributed to one of several intrinsic effects, such as electromigration [35], an increase in point defect concentration [36], and/or enhanced defect mobility [37]. The electromigration theory suggests that the increase in the flux of the diffusion of atoms is a result of the momentum transfer from the "electron wind" effect [38]. Bertolino *et al.*, [39, 40] studied the electromigration effects on the Au-Al multilayer systems, which showed that the electric current increases the rate of product layer formation and decrease the incubation time for the nucleation of a new phase. The findings of Bertolino *et al.*, [39] suggested that the effect of the electrical current in the EFAS process was attributed to electromigration by observing the fracture surface of the necks formed in Cu particles under high electrical currents.

In this research, the intrinsic role of electrical current during the EFAS process of stainless steel nanoparticles was investigated by both *ex situ* and *in situ* EFAS experiments. The studies of the fundamental mechanisms were made possible by using a novel device on the Si chip that was specifically designed and fabricated to fit into the TEM sample holder. The combination of the microstructural observations by electron microscopy and electrical measurements revealed the controlling mechanisms during different stages of the EFAS process of stainless steel nanoparticles.

2. Experimental

Stainless steel 316L (SS316L) nanoparticles with a nominal composition of 65wt%

Fe, 17wt% Cr, 14wt% Ni, 2wt% Mo, 1.5 wt% Mn, and 0.01 wt% C were purchased from US Research Nanomaterials. They are spherical nanoparticles with an average diameter of 80 nm. Two transmission electron microscopies were used in this study. The FEI Tecnai Osiris S/TEM operated at 200 kV was used for bright field (BF) transmission electron microscopy (TEM) imaging and energy-dispersive spectrometry (EDS). The JEOL 2010 LaB₆ TEM was used for *in situ* EFAS experiments. 0.5 grams of as-received SS316L nanoparticles were dispersed in 10 mL ethanol by an ultrasonic bath for 15 minutes at room temperature. Then the suspension of nanoparticles was ready for drop-casting on a silicon (Si) chip.

A unique device on the Si chip has been designed and fabricated to conduct the EFAS experiments, including *ex situ* and *in situ* EFAS experiments. The schematic diagram of this unique device is shown in Figure 1. The Si chip with a window was used as the substrate (**Figure 1a**). Silicon nitride (Si₃N₄) film with a thickness of 50 nm was deposited on Si wafer by chemical vapor deposition (CVD) method. The observation windows were prepared by etching Si using 33 weight. % KOH solution, leaving Si₃N₄ membranes in the windows [41]. The Si₃N₄ membrane was 50 nm thick and transparent to the electron beam. Platinum (Pt) electrodes were electron-beam evaporated on top of the Si chip and Si₃N₄ film for electrical connection (**Figure 1c**).

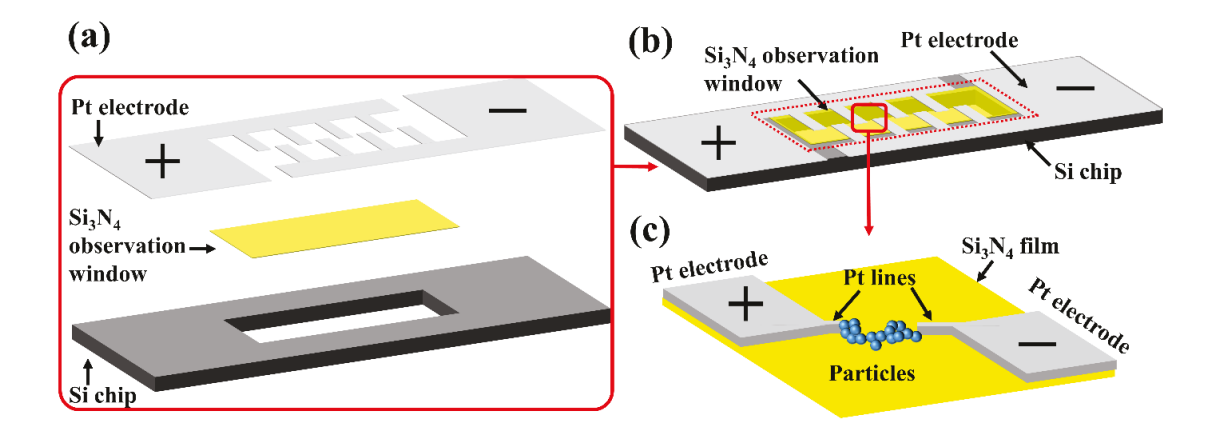


Figure 1. Schematic diagram of a unique device on the Si chip for *in situ* transmission electron microscopy (TEM) sintering experiments. (a) exploded view of the three layers of the device; (b) schematic of the device; (c) a chain of stainless steel 316L (SS316L) nanoparticles on the Si₃N₄ film and connected to Pt electrodes.

This device was specifically designed to fit into a single tilt TEM sample holder (Gatan Model 672, Gatan Inc.). **Figure 2a** shows the photo of the Si chip on the TEM sample holder. Two screws were used to hold the Si chip and connect with the TEM holder. **Figures 2b** shows the SEM image of Pt electrodes and Si₃N₄ observation windows on the Si chip. SS316L nanoparticles were dispersed between the small gaps between Pt electrodes (**Figure 2c**).

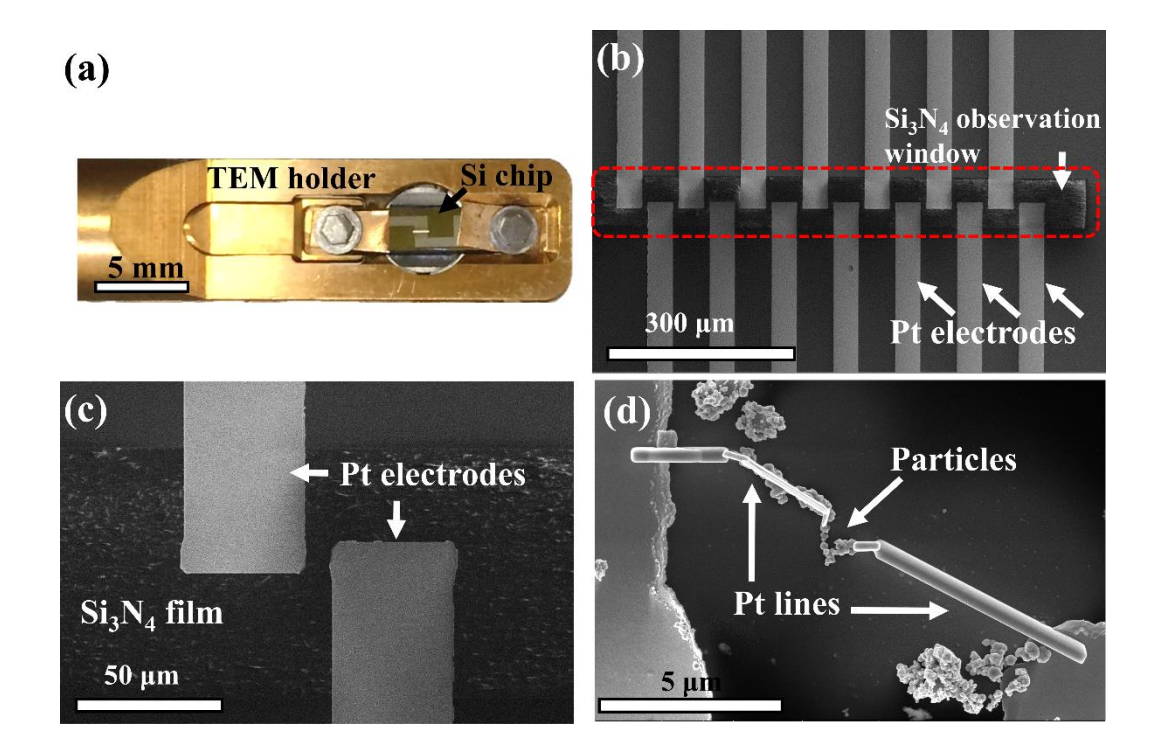


Figure 2. (a) Photo of the Si chip in a TEM holder (Gatan Model 672). (b) Scanning electron microscopy (SEM) image of the distribution of Pt electrodes and Si₃N₄ observation window on the Si chip. (c) SEM image of the enlarged view of the gap between Pt electrodes. (d) SEM image of SS316L nanoparticles connected to the Pt electrodes by electron beam deposited Pt lines.

The SS316L nanoparticles in ethanol solution were drop-casted on the Si₃N₄ film region (**Figure 1b**) and dried in an ambient environment. The electron beam deposition of Pt was used to connect a group of stainless steel particles with Pt electrodes, which was conducted at the FIB/SEM system (Helios 660, FEI Company). **Figure 2d** shows the SEM image of SS316L nanoparticles, which were connected to the Pt electrodes by electron beam deposited Pt lines.

The EFAS experiments of SS316L nanoparticles were conducted by applying an electrical current through the silicon chip in the TEM sample holder. An electrical source meter (Keithley 2400, Tektronix, Inc.) was used to generate, control and accurately measure the electrical voltage and current signals during the sintering experiments. The electrical resistance was calculated based on Ohm's law. Both ex situ and in situ EFAS experiments were carried out by using the silicon chip device to study the mechanisms during the electric field assisted sintering process. The ex situ EFAS experiments were carried out outside a TEM system. Scanning electron microscopy (SEM, Helios 660, FEI Company) was used to observe the morphology of SS316L nanoparticles during the interruption of the ex situ sintering experiments. The chemical composition was analyzed by EDS. The focused ion beam (FIB) process was also conducted in the Helios 660. The *in-situ* EFAS experiments were carried out in the transmission electron microscope (2010 LaB₆, JEOL) operated at 200 kV. Bright-field transmission electron microscopy (TEM) images were acquired to characterize the microstructural changes of nanoparticles. The dynamic sintering process of SS316L nanoparticles was recorded as videos using a charge-coupled device (CCD) camera with a recording rate of 50 frame-per-second (fps).

3. Results and discussion

Figure 3 shows the TEM characterizations of the as-received SS316L nanoparticles. In the HRTEM image of a SS316L nanoparticle (Figure 3b), the measured d-spacing

of (1 1 1) plane, $d_{(111)} = 2.08\text{Å}$, is consistent with the lattice parameter of SS316L. An ultra-thin layer of oxide film was present on the surface of SS316L nanoparticles, which was revealed by the high-resolution TEM images (e.g., Figure 3b). The average thickness of the oxide film, measured from 15 SS316L nanoparticles, was 3.9 ± 0.5 nm. According to EDS analysis, the chemical composition of the oxide film is 20-25% O, 20-40% Fe, 5-25% Cr, 28-34% Ni, 2-5% Mn, and 0-1% Mo in atomic percent. This ultra-thin oxide film may be formed by oxidation at room temperature when the stainless steel particle was exposed to air [42]. Figure 3c shows a high-angle annular dark-field (HAADF) image of the SS316L nanoparticle, in which the oxide film has a darker contrast due to its lower average atomic number. Figures 3d to 3g are the corresponding EDS mapping results of O, Fe, Cr, and Ni elements, respectively. The O element enrichment indicates the oxide film, while the enrichment of Fe, Cr, and Ni elements indicate the SS316L nanoparticle.

The electrical resistivity of SS316L is $7.2\times10^{-7}\,\Omega$ m [43], while the electrical resistivity of the oxide layer is 1.0 to $6.9\times10^{-4}\,\Omega$ m [44]. Thus, the oxide film has a much higher electric resistance than the SS316L particle, and can thus become a strong barrier for electrical conduction between SS316L particles during the EFAS process. The electrical resistance of the contact point between the Pt electrode and SS316L nanoparticles was estimated to be less than $100\,\Omega$, which is much lower than the total electric resistance ($\sim10^6\,\Omega$) and thus can be ignored.

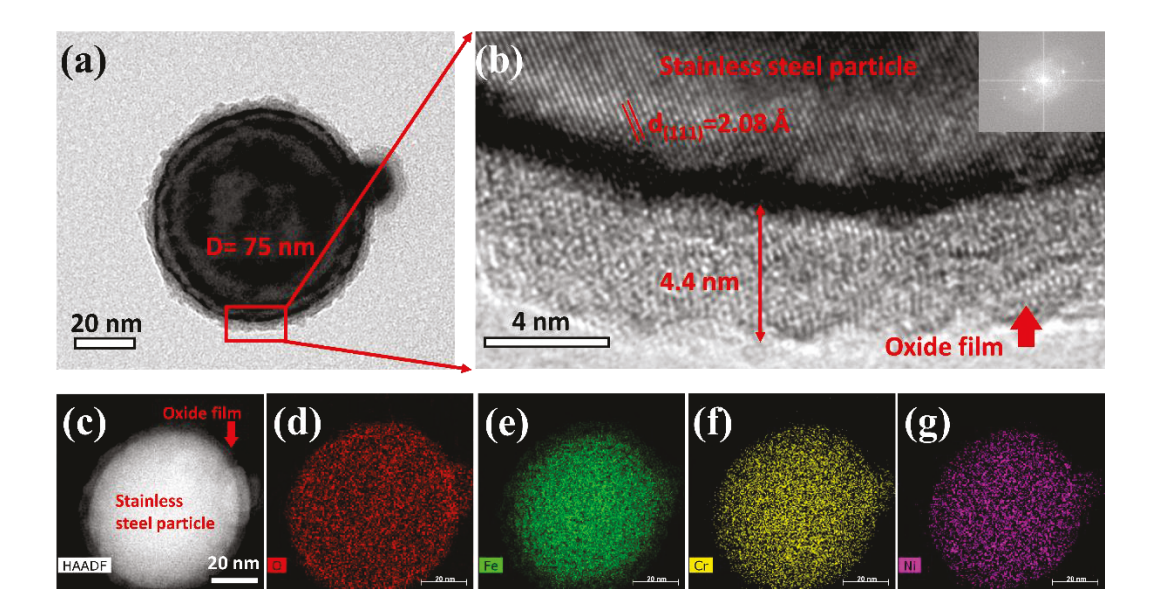


Figure 3. (a) TEM image of an SS316L nanoparticle. D= diameter. (b) High-resolution TEM image showing an ultra-thin oxide film (4-5 nm thick) on the surface of SS316L nanoparticle. (c) HAADF image of a SS316L nanoparticle with (d)-(g) the corresponding EDS mapping of O, Fe, Cr, and Ni elements, respectively.

3.1 Ex situ EFAS experiments

During the *ex situ* EFAS experiments, the change of voltage and current during the sintering process was recorded in real time, while the morphology change of SS316L nanoparticles was observed *ex situ* by SEM during the interruption of the EFAS experiments.

The sintering process of SS316L nanoparticles was controlled by the voltage input.

The voltage was raised stepwise from 0, 1.5V, 3V, to 4.5V. During the sintering process, the voltage stayed at 1.5V for 400s, at 3V for 260s, and at 4V for 130s. The

measured electric current increased with the voltage and then showed slightly fluctuations at 1.5V and 3V and more significant fluctuations when the voltage was raised to 4.5V (**Figure 4a**). The fluctuation of the measured electrical current suggested the local change of the electrical resistance of SS316L nanoparticles. A similar phenomenon of electrical current variation was observed during the EFAS of Ni nanoparticles [33]. SEM images of SS316L nanoparticles before and after the initial sintering at 4.5V are presented in **Figure 4b** and **Figure 4c**, respectively. The overall morphology of SS316L nanoparticles remained the same. However, local microstructural changes are observed to occur at the interface of nanoparticles. For example, the tangential interface between some nanoparticles became a closer and adjacent boundary after sintering at 4.5V (e.g., Locations 1 and 2), and the gap between some particles became smaller and connected (e.g., Location 3 and 4).

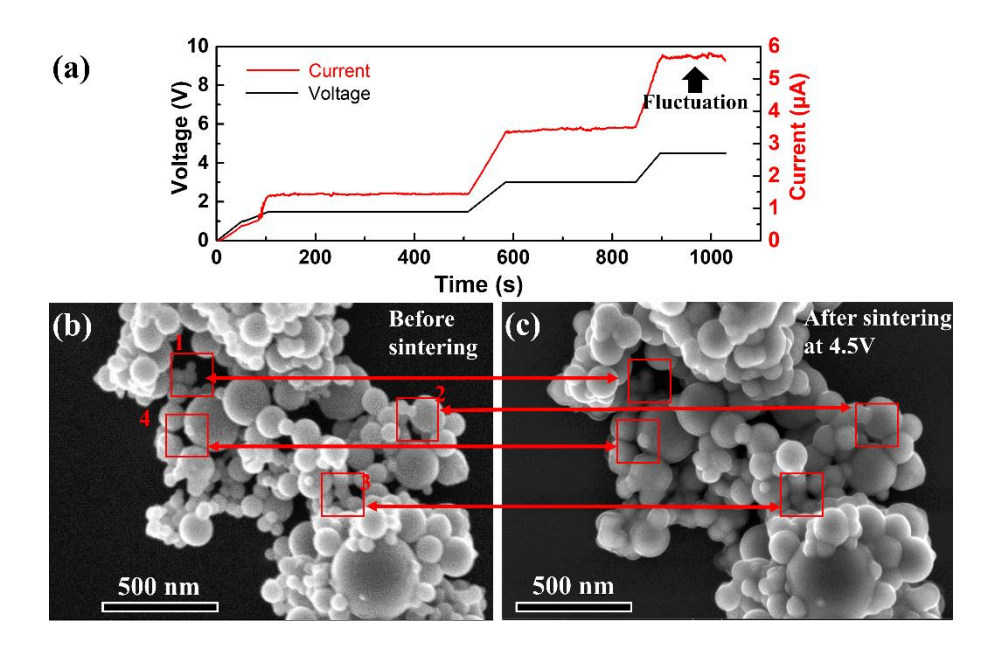


Figure 4. (a) The measured electrical current as a function of time with the stepwise increase of the applied electrical voltage to 4.5V. SEM images of the SS316L particles (b) before and (c) after the initial sintering at 4.5V.

At the early stage of the EFAS process, the fluctuation of the measured electrical current may be related to the electric current cleaning of oxide film on the surface of SS316L nanoparticles. The SS316L particles were covered by an ultra-thin layer of oxide film (Figure 3) with a higher electrical resistance than SS316L. Chaim [32] suggested that the local electrical field intensification at the contact region of the particles can contribute to the electric current cleaning and dielectric breakdown of the oxide film. The applied electric field was assumed to cause the polarization of the oxide layer and migration of oxygen anions away from the contact region of the particles, resulting in disruption of the oxide film on metal particles [45], although further experiments are necessary to verify this effect. When the oxide film was disrupted until completely removed, the direct connection of SS316L nanoparticles without oxide films can lower the local electrical resistance, leading to a slight rise of electrical current. Meanwhile, the formation of a good connection between these nanoparticles can cause a slight shrinkage of the gap between them, which can also result in a worse contact of these particles with other particles leading to another slight reduction of electric current. These local effects can cause the fluctuation of the measured electrical current in the electric current vs. time curve (Figure 4a). The

microstructural changes of SS316L nanoparticles after the initial sintering at 4.5V indicate that both the direct connection of SS316L nanoparticles and the slight shrinkage of the gap between nanoparticles (Figure 4c) occurred during the fluctuation of the measured electrical current. Thus, the microstructural observations provide the experimental evidence to support the above mechanisms, which suggest the electron current fluctuation corresponds to the removal of surface oxide film and connection between SS316L particles at the early stage of the EFAS process.

The second sintering experiment was performed on the same group of particles at higher electrical voltages. The electrical voltage was raised stepwise at 2.5V for each step. The measured electric current slowly increased with the voltage and showed fluctuations (**Figure 5a**). When the electrical voltage was at 20V, a sudden "leap" of electrical current occurred when the electrical current increased abruptly from 20 to over $60 \, \mu A$ in 1.5 seconds. There is a sudden drop in electrical current after the 'leap' due to the loss of connection after the consolidation, but the electrical current did not drop to zero (see the inset image in Figure 5a).

SEM images of SS316L nanoparticles before and after the second sintering at 20V are presented in **Figure 5b** and **Figure 5c**, respectively. The as-casted SS316L nanoparticles formed a chain between two Pt electrodes (Figure 5b). After the second sintering at 20V, SS316L nanoparticles were completely consolidated into four larger particles (Figure 5c) that were adhered to Pt electrodes. The complete consolidation was so abrupt and intense that it broke the supporting Si₃N₄ film. Another possibility

is that the local areas in the Si₃N₄ thin film might have gathered a large amount of heat in a very short time, making it to break down. However, this cannot be verified because there is no sensor in this device to measure the local temperature of the Si₃N₄ film. EDS mapping of Fe, Cr, and Ni elements (**Figure 5d**) confirm that the four large particles ("1" to "4") in Figure 5c are the sintered SS 316L. The borders of Pt electrodes before and after sintering are marked by yellow dashed lines (Figure 5b and 5c). No obvious change occurred in the Pt electrodes after sintering. However, EDS analysis suggested that there was a thin Pt coating (marked by the green dashed line in Figure 5c) deposited on the Si₃N₄ film that connects the two Pt electrodes after sintering. The thin conductive layer of Pt coating on the Si₃N₄ film may contribute to the nonzero final electric current after sintering.

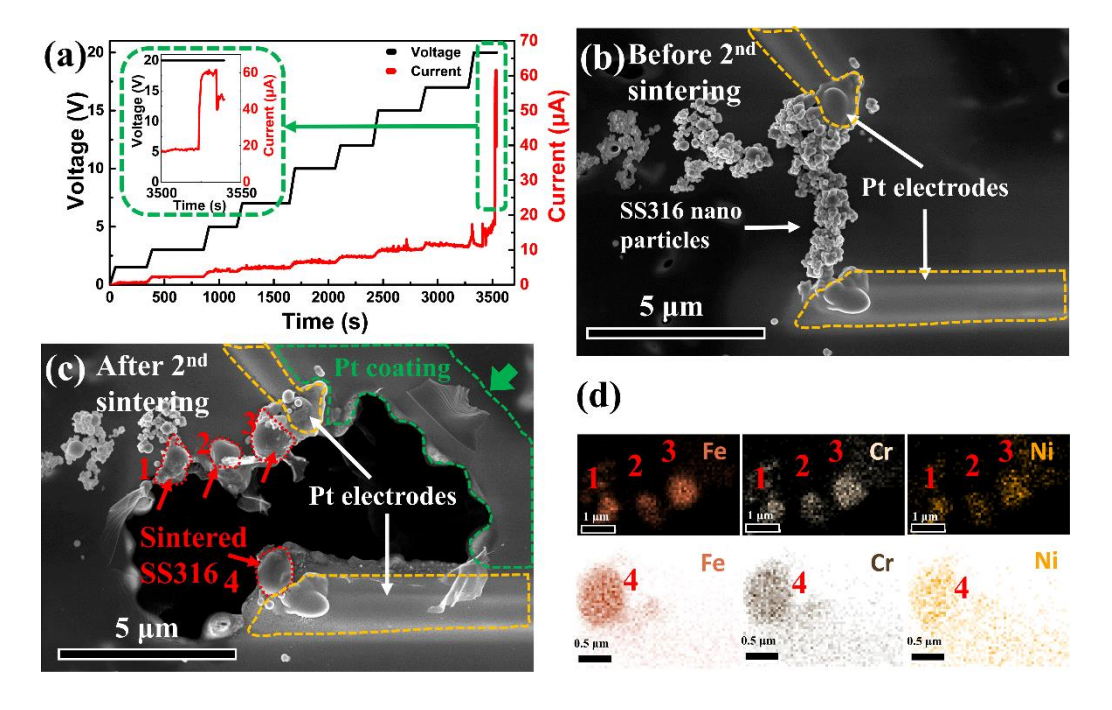


Figure 5. (a) The measured electrical current as a function of time with the stepwise increase of the applied electrical voltage to 20V. Insert: the enlarged view of the sudden changes of electrical current near 20 V. SEM image of SS316L nanoparticles (b) before and (c) and after the second sintering at 20V. The group of SS316L nanoparticles was connected to Pt electrodes. (d) EDS mapping of the distribution of the Fe, Cr, and Ni elements after the second sintering at 20V.

3.2 In situ EFAS experiments

To better understand the correlation between the electrical behavior and microstructural changes of SS316L nanoparticles during the EFAS process, *in situ* TEM experiments were conducted to allow real-time observation of the microstructural evolution of SS316L nanoparticles as well as electrical property changes simultaneously.

The voltage on the SS316L nanoparticles was raised linearly from 0 to 8 volts at a constant rate of 0.2 V/s. **Figure 6a** and **6b** show bright-field TEM images of SS316L nanoparticles before sintering (t₁=0 s, at 0 V) and at t₂=36.99 s (corresponding to 7.4 V). An enlarged view of the local microstructural features in Figures 6a and 6b is presented and compared in Figure 6a_i and 6b_i (i=1, 2, 3), respectively. The comparison of Figure 6a₁ and 6b₁ indicated a small nanoparticle (arrowed) might have been "dissolved" by a larger nanoparticle. The comparison of Figure 6a₂ and 6b₂, as well as that of Figure 6a₃ and 6b₃, suggested the development of necks (arrowed) between the

adjacent nanoparticles. All these microstructural observations showed that the sintering of nanoparticles was in progress, involving the coalescence of nanoparticles through neck formation, as well as the Ostwald ripening (small nanoparticles dissolved and re-deposited onto larger nanoparticles). The neck formation can allow more electric current to pass through two neighboring nanoparticles, resulting in a lower local electrical resistance. The electric current measurement showed that from t₁=0 s to t₂=36.99 s, the electric current was slowly increased with the electric current (Figure 6d), while the electrical resistance was significantly decreased from about 140 k Ω to 70 k Ω (**Figure 6e**). Such consistency indicates the microstructural changes observed in Figure 6b_i (i=1, 2, 3) may be driven by the mass transport enhanced by electrical currents [39, 40]. It is important to note that the measured electric current experienced two stages: a slow rate of current increase from 0 to 17s (corresponding to 3.4V), while a higher rate from 17 to 36.99s. Such electric current behavior implied that the neck growth between adjacent nanoparticles became faster when the voltage is higher than 3.4 V.

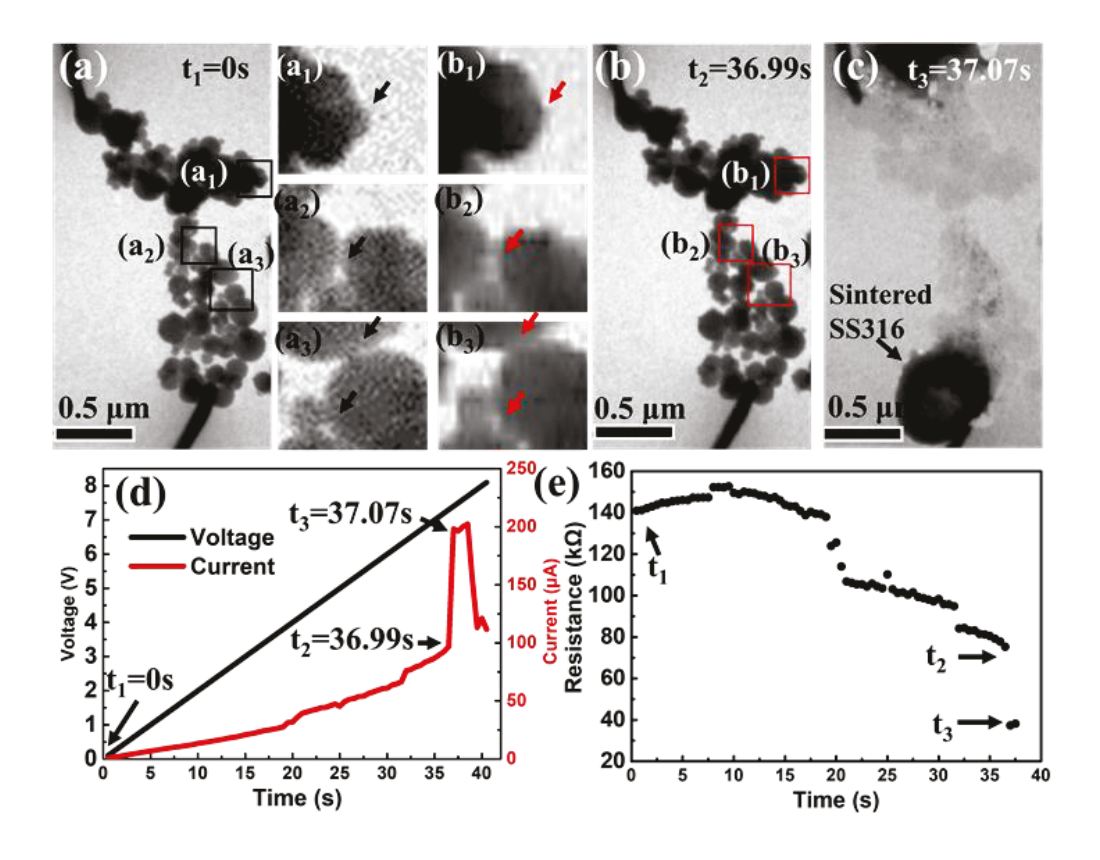


Figure 6. Bright-field TEM images of SS316L nanoparticles of (a) before sintering; (b) at t₁=36.99 seconds (corresponding to 7.4 V); and (c) at t₂=37.07 seconds. The features of microstructural changes are compared between (a_i) and (b_i), i=1, 2, 3. (d) The measured electrical current as a function of time with the linear increase of the applied electrical voltage at a constant rate of 0.2 V/s. (e) Evolution of electrical resistance as a function of time.

From t_2 =36.99 s to t_3 =37.07 s, a fast consolidation suddenly occurred in this chain of SS316L nanoparticles (**Figure 6c**). It is noticed that the shadow of nanoparticles was still present in Figure 6c due to the image persistence effect. The recording rate of the video was limited by the CCD camera to be 50 fps, equivalent to 0.02 seconds per frame. The consolidation process of nanoparticles was not captured by the video,

suggesting that it occurred within a very short period of less than 0.02 seconds. Meanwhile, the electrical current measurement showed that from t_2 =36.99 s to t_3 =37.07 s, an abrupt leap of the electric current occurred at 7.4 V (Figure 6d). The electrical resistance was also abruptly reduced from about 75.3 k Ω to 37.3 k Ω (Figure 6e). The peak of electrical current was followed by a sudden drop (open circuit) after sintering (Figure 6c). Similar to Figure 5, the nonzero final electric current may be also explained by the thin conductive Pt coating on the Si₃N₄ thin film.

To study the evolution of oxide layer of particles during the EFAS process, another group of SS316L nanoparticles was *in situ* sintering in the TEM. Figure 7a and 7b show the formation of necks between the adjacent particles after sintering. The sintering process was interrupted after necks were formed, so that the composition of necks could be analyzed to verify the removal of oxide layers in SS316L nanoparticles during the EFAS process.

These particles were transferred to another TEM (FEI Tecnai Osiris S/TEM) that is installed with an EDS detector by the focused ion beam lift-out technique [46]. Figure 7c below shows the cross-section view of the particles after sintering. Two particles, P1 and P2, formed a neck. The particles were surrounded by an oxide layer before sintering. Figure 7d is an enlarged view of the neck of the two particles, which clearly shows that the neck is free of oxide layers. To verify the removal of oxide layer in the neck region, EDS line scan was performed along the white dotted line in Figure 7c. Figure 7e shows the EDS line scan profiles of O, Fe, Cr and Ni element distribution.

The oxygen peak at ~10 nm corresponds to the oxide layer of P1. In contrast to the oxygen peak in the oxide layer of P1, there was no oxygen peak at the neck of two particles. Thus, the combination of TEM images and oxygen element distribution proved that the removal of oxide layer occurred in the neck region between two particles during sintering during the EFAS process.

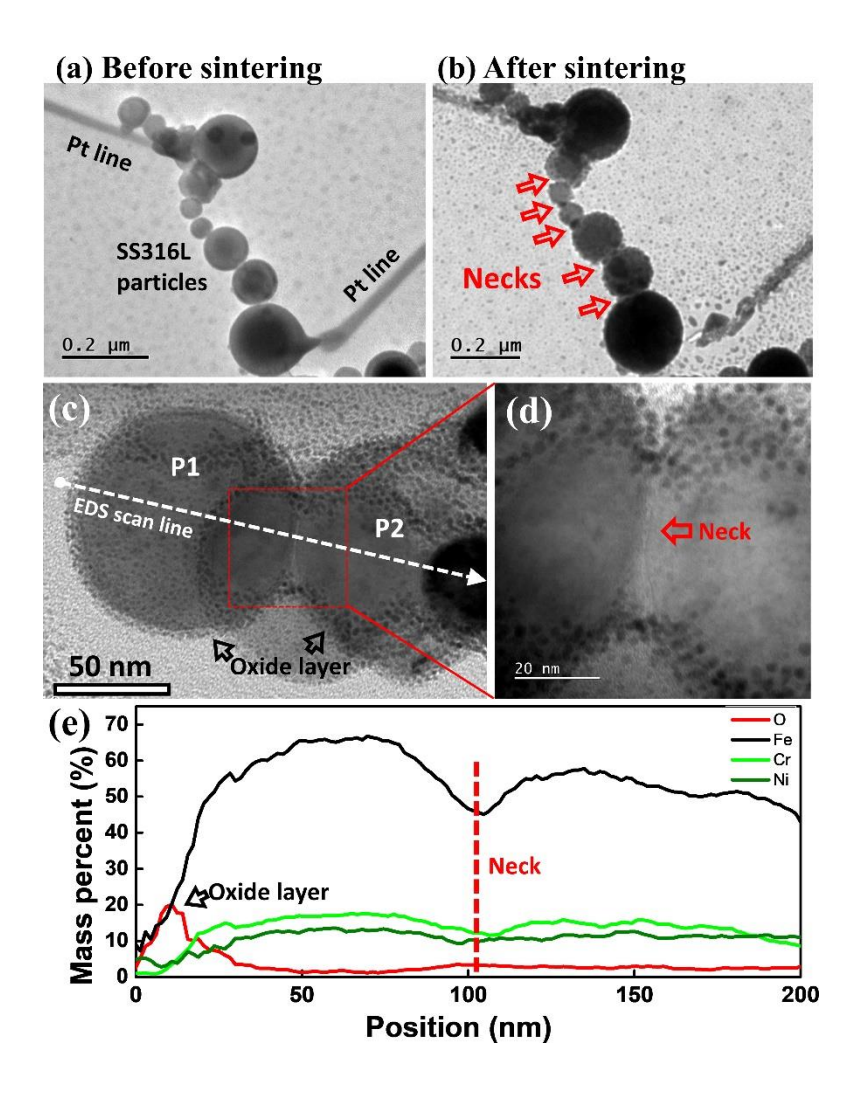


Figure 7. (a, b) TEM images showing the formation of necks between SS316L particles after EFAS. (c) Cross-section view of two particles (P1 and P2) after sintering; (d) an enlarged view of the interface between the two particles; (e) EDS line

scan profiles of O, Fe, Cr and Ni elements distribution along the white dotted line in

c).

3.3 Preliminary mechanisms of EFAC process of 316L nanoparticles

The following preliminary mechanisms can be proposed to be the most likely mechanisms for the EFAC process of 316L nanoparticles based on the current microscopy observations and electrical measurements in both *ex situ* and *in situ* EFAC experiments as well as the literatures. These experiments suggest that the EFAC process of 316L nanoparticles may experience four stages that are schematically illustrated in **Figure 8**, involving the initial electric current cleaning of the oxide film, subsequent neck formation, neck growth, and the final fast consolidation.

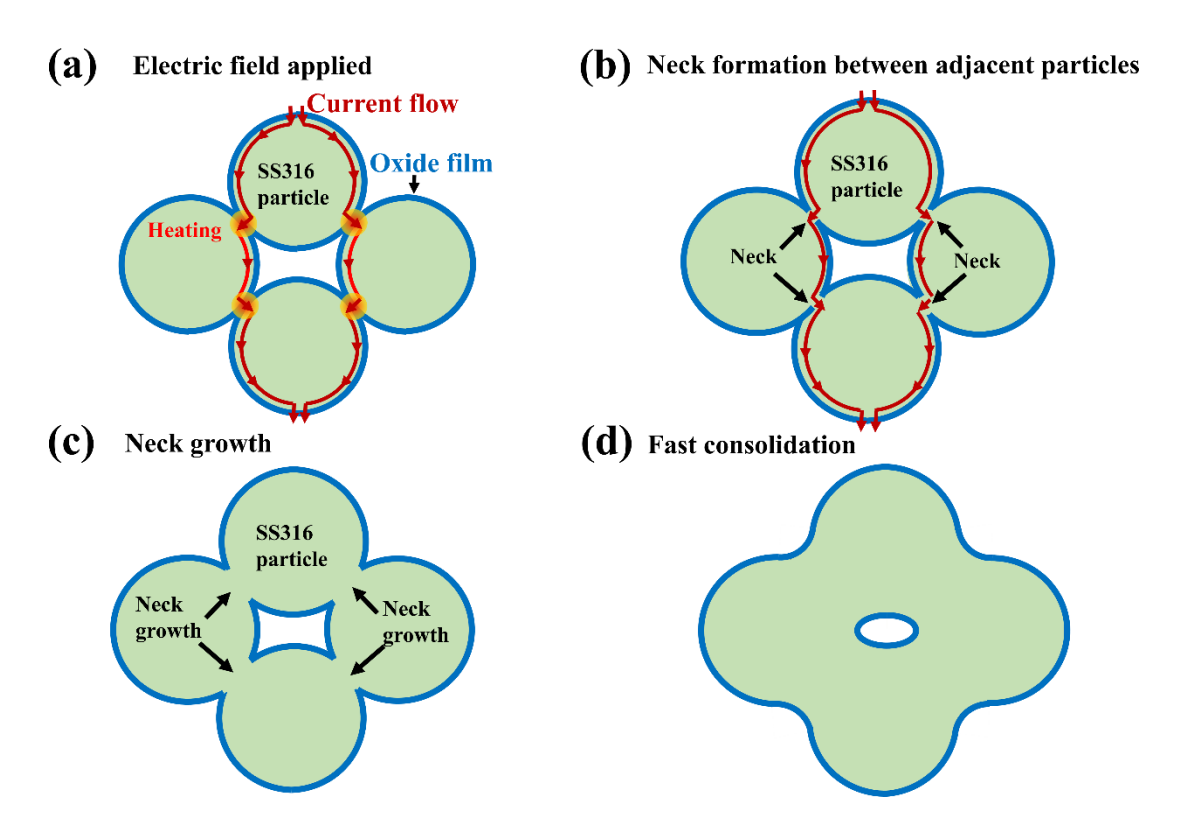


Figure 8. Schematic illustration of the four stages of the EFAC process of SS 316L nanoparticles: (a) cleaning of oxide film on the surface of nanoparticles by electric

currents; (b) neck formation between the adjacent SS 316L nanoparticles; (c) neck growth between SS 316L nanoparticles; and (d) fast consolidation.

1st stage (Figure 8a): cleaning of oxide film on the surface of nanoparticles by electric currents. SS316L nanoparticles were covered by a thin (several nanometers) layer of oxide film, which was a barrier to electrical conduction. When an electrical voltage was applied, a small leakage current can occur in the thin oxide film due to the tunneling effect of the defect structures in the oxide film [47]. With the aid of electric current, the diffusion of oxygen was enhanced by the generation of oxygen vacancies as well as the migration of oxygen anions [48]. Oxygen diffused away from the contact region of two particles, resulting in the disruption and gradual removal of the oxide film on metal particles [45, 49]. With the increase of the applied voltage, the electric field intensification at the inter-particle contact areas can also lead to the dielectric breakdown of the oxide film [32]. These physical processes may contribute to the electrical current cleaning of the oxide film on the surface of SS 316L nanoparticles at the contact region of two particles (Figure 7c-7e).

2nd stage (Figure 8b): neck formation between the adjacent SS 316L nanoparticles. When the thin oxide film on the surface was removed, a direct metallic connection forms between the adjacent SS316L nanoparticles. Joule heating at the connection point of particles can also promote the formation of metallic necks between adjacent particles [48]. The neck formation between the adjacent SS 316L nanoparticles was

observed in both *ex situ* (Figure 4c) and *in situ* (Figures 6b and 7b) EFAS experiments. Once a neck was formed, a favorable path of the electrical current was created, which can cause a decrease in the local electrical resistance and, thus, a jump of electrical current (Figure 4a and 6d).

3rd stage: neck growth between SS 316L nanoparticles. The growth of the neck may be driven by the mass transport enhanced by electrical currents. The enhanced mass transport may be attributed to one of several intrinsic effects, such as electromigration [39, 50], an increase in point defect concentration [51], and/or enhanced defect mobility [37]. In the electromigration, the increase in the flux of the diffusion of atoms is a result of the momentum transfer from the "electron wind" effect [7, 52]. According to the electromigration theory, an electric current passing through the sample can cause an added driving force to the chemical potential for mass transport, such that the flux can be expressed by [25]:

$$J_i = -\frac{D_i C_i}{RT} \left[RT \frac{\partial \ln C_i}{\partial x} + F z^* E \right] \tag{1}$$

where J_i is the flux of the ith species, D_i is the diffusivity of the species, C_i is the concentration of the species, R is the gas constant, T is the temperature, F is Faraday's constant, z^* is the effective change on the diffusing species, and E is the electric field. [24] studied the effect of electrical current using the sintering of copper spheres to copper plates as the model, which showed the increase in the diameter of the neck with an increase in the current.

4th stage: fast consolidation. In the final stage of the sintering process, the fast consolidation of SS 316L nanoparticles was observed in both ex situ (Figure 5c) and in situ (Figure 6c) EFAS experiments. The fast consolidation was always accompanied by an abrupt "leap" of the electric current or reduction of the electrical resistance. Combining the simultaneous microstructural observations and electrical measurements, the fast consolidation may be explained by the following mechanisms. In the final stage of the EFAS process, the large necks between the SS316L nanoparticles may have created a "short circuit" route for the electrical flow, leading to a rapid increase of electrical current. The high electrical current can significantly accelerate the mass transport between the nanoparticles and can also induce significant Joule heating resulting in the local melting of the small nanoparticles [48, 53]. These physical processes may contribute to the fast consolidation of SS316L nanoparticles.

In the four-stage process, the first three stages appeared to occupy most of the time of the EFAS process of SS 316L nanoparticles, while the final consolidation was completed in a very short period of time (less than 0.02 seconds). The proposed EFAS mechanisms for stainless steel nanoparticles may aid the understanding of the EFAS mechanisms of other metallic materials as well as the mechanisms in the advanced manufacturing process such as SPS or PECS.

4. Conclusions

The intrinsic role of electrical current on the EFAS process of stainless steel 316L nanoparticles was revealed by both ex situ and in situ experiments. A novel device on the Si chip was designed and fabricated to fit into the TEM sample holder to carry out these experiments, which allows for the observation of the microstructural evolution of nanoparticles combined with the simultaneous measurement of electrical voltage and current and changes. These experiments suggested that the EFAC process of 316L nanoparticles may experience four stages, involving the initial electric current cleaning of the oxide film, subsequent neck formation, neck growth, and the final fast consolidation. SS 316L nanoparticles were covered by a thin (several nanometers) layer of oxide film, which was removed by electrical current cleaning. Consequently, a metallic neck formed between the adjacent SS316L nanoparticles, creating a favorable path of the electrical current. The growth of the neck may be driven by the mass transport enhanced by electrical currents, which finally led to the fast consolidation of SS316L nanoparticles. The first three stages occupied most of the time of the EFAS process, while the final consolidation was completed in a very short period.

Acknowledgment

This material is based upon work supported by the National Science Foundation under Grant No. CMMI-1762190. Manufacturing and characterization analyses were performed at the NanoEngineering Research Core Facility (part of the Nebraska

Nanoscale Facility), which is partially funded from the Nebraska Research Initiative.

The research was performed in part in the Nebraska Nanoscale Facility: National

Nanotechnology Coordinated Infrastructure and the Nebraska Center for Materials

and Nanoscience, which are supported by the National Science Foundation under

Award ECCS: 1542182, and the Nebraska Research Initiative.

Declaration of interest - None

References

- 1. German R M, 1996, SINTERING THEORY AND PRACTICE. John Willey Son N Y
- 2. Rahaman MN (2010) 2 Kinetics and mechanisms of densification. In: Fang ZZ (ed) Sintering of Advanced Materials. Woodhead Publishing, pp 33–64
- 3. Guillon O, Gonzalez-Julian J, Dargatz B, et al (2014) Field-Assisted Sintering Technology/Spark Plasma Sintering: Mechanisms, Materials, and Technology Developments. Adv Eng Mater 16:830–849. https://doi.org/10.1002/adem.201300409
- 4. Hsueh CH, Evans AG, Coble RL (1982) Microstructure development during final/intermediate stage sintering—I. Pore/grain boundary separation. Acta Metall 30:1269–1279
- 5. Curran DJ, Fleming TJ, Towler MR, Hampshire S (2010) Mechanical properties of hydroxyapatite–zirconia compacts sintered by two different sintering methods. J Mater Sci Mater Med 21:1109–1120. https://doi.org/10.1007/s10856-009-3974-z
- 6. Niittynen J, Abbel R, Mäntysalo M, et al (2014) Alternative sintering methods compared to conventional thermal sintering for inkjet printed silver nanoparticle ink. Thin Solid Films 556:452–459

- 7. Wang H, Kou R, Harrington T, Vecchio KS (2020) Electromigration effect in Fe-Al diffusion couples with field-assisted sintering. Acta Mater 186:631–643. https://doi.org/10.1016/j.actamat.2020.01.008
- 8. Calvert EL, Knowles AJ, Pope JJ, et al (2019) Novel high strength titanium-titanium composites produced using field-assisted sintering technology (FAST). Scr Mater 159:51–57. https://doi.org/10.1016/j.scriptamat.2018.08.036
- 9. Grasso S, Sakka Y, Maizza G (2009) Electric current activated/assisted sintering (ECAS): a review of patents 1906–2008. Sci Technol Adv Mater 10:053001
- 10. Guillon O, Gonzalez-Julian J, Dargatz B, et al (2014) Field-assisted sintering technology/spark plasma sintering: mechanisms, materials, and technology developments. Adv Eng Mater 16:830–849
- 11. Yan X, Wang F, Hattar K, et al (2019) Novel amorphous SiOC dispersion-strengthened austenitic steels. Materialia 6:100345
- 12. Zhou Y, Hirao K, Yamauchi Y, Kanzaki S (2004) Densification and grain growth in pulse electric current sintering of alumina. J Eur Ceram Soc 24:3465–3470
- 13. Groza JR, Zavaliangos A (2000) Sintering activation by external electrical field. Mater Sci Eng A 287:171–177. https://doi.org/10.1016/S0921-5093(00)00771-1
- 14. Biesuz M, Rizzi D, Sglavo VM (2019) Electric current effect during the early stages of field-assisted sintering. J Am Ceram Soc 102:813–822. https://doi.org/10.1111/jace.15976
- 15. Guillon O, Gonzalez-Julian J, Dargatz B, et al (2014) Field-assisted sintering technology/spark plasma sintering: mechanisms, materials, and technology developments. Adv Eng Mater 16:830–849
- 16. Biesuz M, Luchi P, Quaranta A, Sglavo VM (2016) Theoretical and phenomenological analogies between flash sintering and dielectric breakdown in α-alumina. J Appl Phys 120:145107
- 17. Langer J, Hoffmann MJ, Guillon O (2009) Direct comparison between hot pressing and electric field-assisted sintering of submicron alumina. Acta Mater 57:5454–5465
- 18. Biesuz M, Sglavo VM (2019) Flash sintering of ceramics. J Eur Ceram Soc 39:115–143
- 19. Yan X, Wang F, Deng L, et al (2018) Effect of Laser Shock Peening on the Microstructures and Properties of Oxide-Dispersion-Strengthened Austenitic Steels. Adv Eng Mater 20:1700641

- 20. Chaim R (2007) Densification mechanisms in spark plasma sintering of nanocrystalline ceramics. Mater Sci Eng A 443:25–32
- 21. Bellosi A, Monteverde F, Sciti D (2006) Fast densification of ultra-high-temperature ceramics by spark plasma sintering. Int J Appl Ceram Technol 3:32–40
- 22. Couret A, Molénat G, Galy J, Thomas M (2008) Microstructures and mechanical properties of TiAl alloys consolidated by spark plasma sintering. Intermetallics 16:1134–1141
- 23. Saheb N, Iqbal Z, Khalil A, et al (2012) Spark plasma sintering of metals and metal matrix nanocomposites: a review. J Nanomater 2012:
- 24. Frei JM, Anselmi-Tamburini U, Munir ZA (2007) Current effects on neck growth in the sintering of copper spheres to copper plates by the pulsed electric current method. J Appl Phys 101:114914
- 25. Munir ZA, Anselmi-Tamburini U, Ohyanagi M (2006) The effect of electric field and pressure on the synthesis and consolidation of materials: A review of the spark plasma sintering method. J Mater Sci 41:763–777
- 26. Munir ZA, Quach DV, Ohyanagi M (2011) Electric current activation of sintering: a review of the pulsed electric current sintering process. J Am Ceram Soc 94:1–19
- 27. Biesuz M, Sglavo VM (2019) Microstructural temperature gradient-driven diffusion: Possible densification mechanism for flash sintering of zirconia? Ceram Int 45:1227–1236
- 28. Orru R, Licheri R, Locci AM, et al (2009) Consolidation/synthesis of materials by electric current activated/assisted sintering. Mater Sci Eng R Rep 63:127–287
- 29. Marder R, Estournès C, Chevallier G, Chaim R (2014) Plasma in spark plasma sintering of ceramic particle compacts. Scr Mater 82:57–60
- 30. Zhang Z-H, Liu Z-F, Lu J-F, et al (2014) The sintering mechanism in spark plasma sintering–proof of the occurrence of spark discharge. Scr Mater 81:56–59
- 31. Hulbert DM, Anders A, Andersson J, et al (2009) A discussion on the absence of plasma in spark plasma sintering. Scr Mater 60:835–838
- 32. Chaim R (2013) Electric field effects during spark plasma sintering of ceramic nanoparticles. J Mater Sci 48:502–510

- 33. Bonifacio CS, Holland TB, van Benthem K (2014) Time-dependent dielectric breakdown of surface oxides during electric-field-assisted sintering. Acta Mater 63:140–149
- 34. Groza JR, Zavaliangos A (2000) Sintering activation by external electrical field. Mater Sci Eng A 287:171–177
- 35. Orchard HT, Greer AL (2005) Electromigration effects on compound growth at interfaces. Appl Phys Lett 86:231906
- 36. Asoka-Kumar P, O'brien K, Lynn KG, et al (1996) Detection of current-induced vacancies in thin aluminum–copper lines using positrons. Appl Phys Lett 68:406–408
- 37. Garay JE, Glade SC, Anselmi-Tamburini U, et al (2004) Electric current enhanced defect mobility in Ni 3 Ti intermetallics. Appl Phys Lett 85:573–575
- 38. Heersche HB, Lientschnig G, O'Neill K, et al (2007) In situ imaging of electromigration-induced nanogap formation by transmission electron microscopy. Appl Phys Lett 91:072107
- 39. Bertolino N, Garay J, Anselmi-Tamburini U, Munir ZA (2001) Electromigration effects in Al-Au multilayers. Scr Mater 44:737–742
- 40. Bertolino N, Garay J, Anselmi-Tamburini U, Munir ZA (2002) High-flux current effects in interfacial reactions in Au–Al multilayers. Philos Mag B 82:969–985
- 41. Vdovin G (1997) Quick focusing of imaging optics using micromachined adaptive mirrors. Opt Commun 140:187–190
- 42. da Cunha Belo M, Walls M, Hakiki NE, et al (1998) Composition, structure and properties of the oxide films formed on the stainless steel 316L in a primary type PWR environment. Corros Sci 40:447–463
- 43. Ali MR, Saka M, Tohmyoh H (2010) Checking Surface Contamination and Determination of Electrical Resistivity of Oxide Scale Deposited on Low Carbon Steel by DC Potential Drop Method. Mater Trans 51:1414–1419
- 44. Peng Y, Park C, Laughlin DE (2003) Fe 3 O 4 thin films sputter deposited from iron oxide targets. J Appl Phys 93:7957–7959
- 45. Bonifacio CS, Holland TB, van Benthem K (2013) Evidence of surface cleaning during electric field assisted sintering. Scr Mater 69:769–772
- 46. Applications of the FIB lift-out technique for TEM specimen preparation Giannuzzi 1998 Microscopy Research and Technique Wiley Online Library. https://onlinelibrary.wiley.com/doi/abs/10.1002/(SICI)1097-

- 0029(19980515)41:4%3C285::AID-JEMT1%3E3.0.CO;2-Q. Accessed 8 Aug 2020
- 47. Watanabe H, Fujita K, Ichikawa M (1998) Observation and creation of current leakage sites in ultrathin silicon dioxide films using scanning tunneling microscopy. Appl Phys Lett 72:1987–1989
- 48. Tseng K-H, Lin P-Y (2014) UNS S31603 stainless steel tungsten inert gas welds made with microparticle and nanoparticle oxides. Materials 7:4755–4772
- 49. Wu M, Yang Y, Yang G, et al (2019) Direct evidence for surface cleaning mechanism during field-activated sintering. J Alloys Compd 784:975–979. https://doi.org/10.1016/j.jallcom.2019.01.035
- Electromigration-Enhanced Densification Kinetics During Spark Plasma Sintering of Tungsten Powder | SpringerLink. https://link.springer.com/article/10.1007/s11661-019-05201-4. Accessed 2 May 2020
- 51. Asoka-Kumar P, O'brien K, Lynn KG, et al (1996) Detection of current-induced vacancies in thin aluminum–copper lines using positrons. Appl Phys Lett 68:406–408
- 52. Landauer R, Woo JW (1974) Driving force in electromigration. Phys Rev B 10:1266
- 53. Serrazina R, Vilarinho PM, Senos AMOR, et al (2020) Modelling the particle contact influence on the Joule heating and temperature distribution during FLASH sintering. J Eur Ceram Soc 40:1205–1211. https://doi.org/10.1016/j.jeurceramsoc.2019.12.015

Figure captions:

Figure 1. Schematic diagram of a unique device on the Si chip for *in situ* transmission electron microscopy (TEM) sintering experiments. (a) exploded view of the three layers of the device; (b) schematic of the device; (c) a chain of stainless steel 316L (SS316L) nanoparticles on the Si₃N₄ film and connected to Pt electrodes.

Figure 2. (a) Photo of the Si chip in a TEM holder (Gatan Model 672). (b) Scanning electron microscopy (SEM) image of the distribution of Pt electrodes and Si₃N₄ observation window on the Si chip. (c) SEM image of the enlarged view of the gap

between Pt electrodes. (d) SEM image of SS316L nanoparticles connected to the Pt electrodes by electron beam deposited Pt lines.

Figure 3. (a) TEM image of an SS316L nanoparticle. D= diameter. (b) High-resolution TEM image showing an ultra-thin oxide film (4-5 nm thick) on the surface of SS316L nanoparticle. (c) HAADF image of an interface between a SS316L nanoparticle with (d)-(g) the corresponding EDS mapping of O, Fe, Cr, and Ni elements, respectively.

Figure 4. (a) The measured electrical current as a function of time with the stepwise increase of the applied electrical voltage to 4.5V. SEM images of the SS316L particles (b) before and (c) after the initial sintering at 4.5V.

Figure 5. (a) The measured electrical current as a function of time with the stepwise increase of the applied electrical voltage to 20V. Insert: the enlarged view of the sudden changes of electrical current near 20 V. SEM image of SS316L nanoparticles (b) before and (c) and after the second sintering at 20V. The group of SS316L nanoparticles was connected to Pt electrodes. (d) EDS mapping of the distribution of the Fe, Cr, and Ni elements after the second sintering at 20V.

Figure 6. Bright-field TEM images of SS316L nanoparticles of (a) before sintering; (b) at t₁=36.99 seconds (corresponding to 7.4 V); and (c) at t₂=37.07 seconds. The features of microstructural changes are compared between (a_i) and (b_i), i=1, 2, 3. (d) The measured electrical current as a function of time with the linear increase of the

applied electrical voltage at a constant rate of 0.2 V/s. (e) Evolution of electrical resistance as a function of time.

Figure 7. (a, b) TEM images showing the formation of necks between SS316L particles after EFAS. (c) Cross-section view of two particles (P1 and P2) after sintering; (d) an enlarged view of the interface between the two particles; (e) EDS line scan profiles of O, Fe, Cr and Ni elements distribution along the white dotted line in c).

Figure 8. Schematic illustration of the four stages of the EFAC process of SS 316L nanoparticles: (a) cleaning of oxide film on the surface of nanoparticles by electric currents; (b) neck formation between the adjacent SS 316L nanoparticles; (c) neck growth between SS 316L nanoparticles; and (d) fast consolidation.

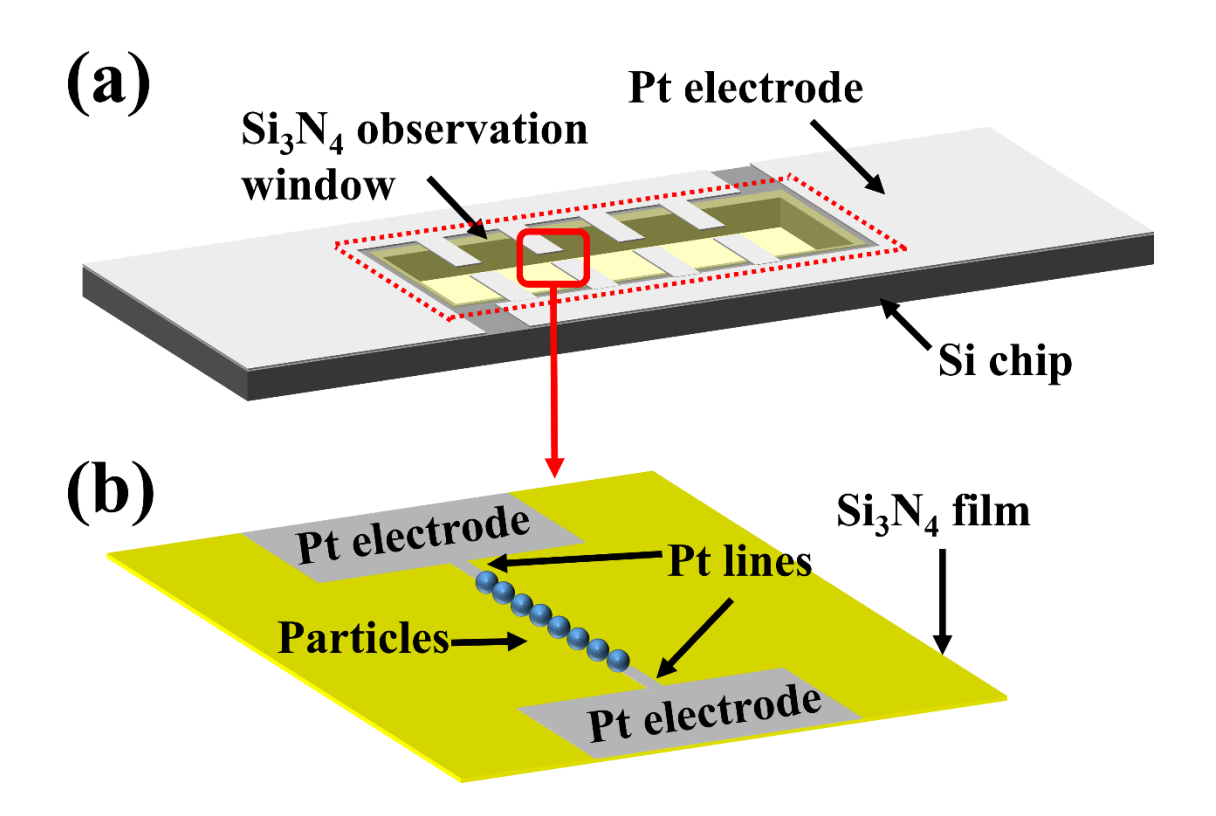


Figure 1. Schematic diagram of a unique device on the Si chip for *in situ* transmission electron microscopy (TEM) sintering experiments. (a) exploded view of the three layers of the device; (b) schematic of the device; (c) a chain of stainless steel 316L (SS316L) nanoparticles on the Si₃N₄ film and connected to Pt electrodes.

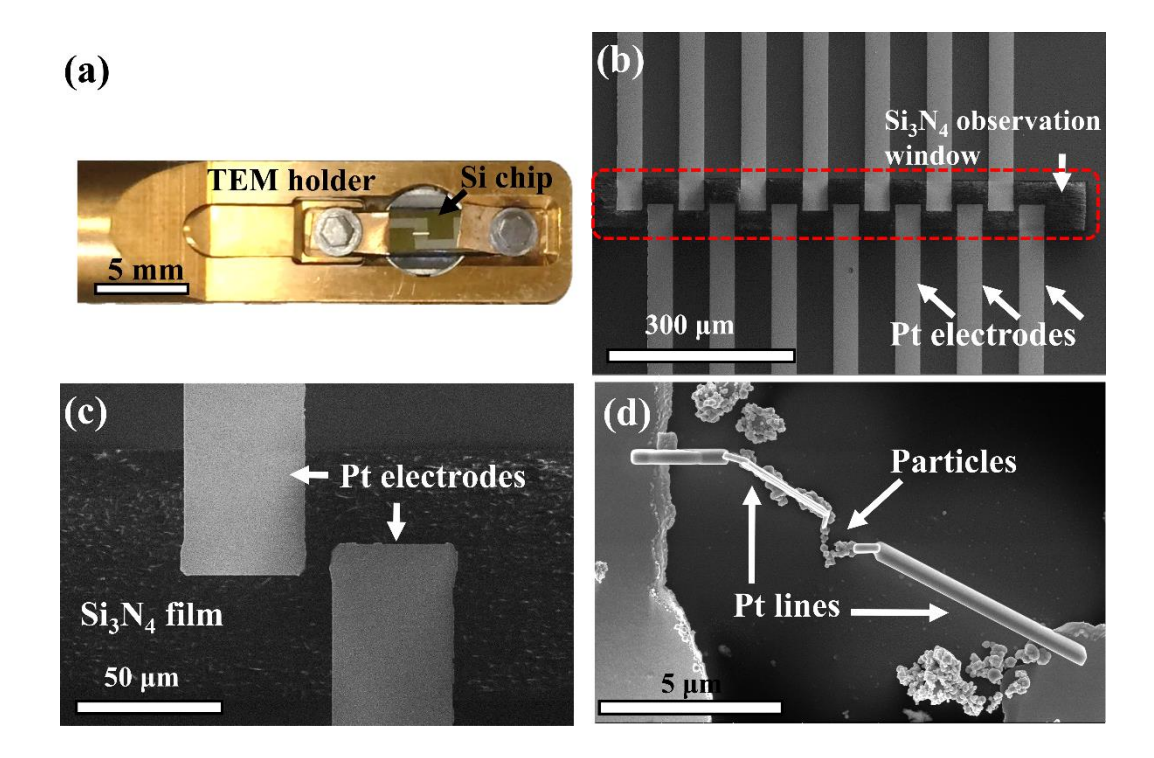


Figure 2. (a) Photo of the Si chip in a TEM holder (Gatan Model 672). (b) Scanning electron microscopy (SEM) image of the distribution of Pt electrodes and Si₃N₄ observation window on the Si chip. (c) SEM image of the enlarged view of the gap between Pt electrodes. (d) SEM image of SS316L nanoparticles connected to the Pt electrodes by electron beam deposited Pt lines.

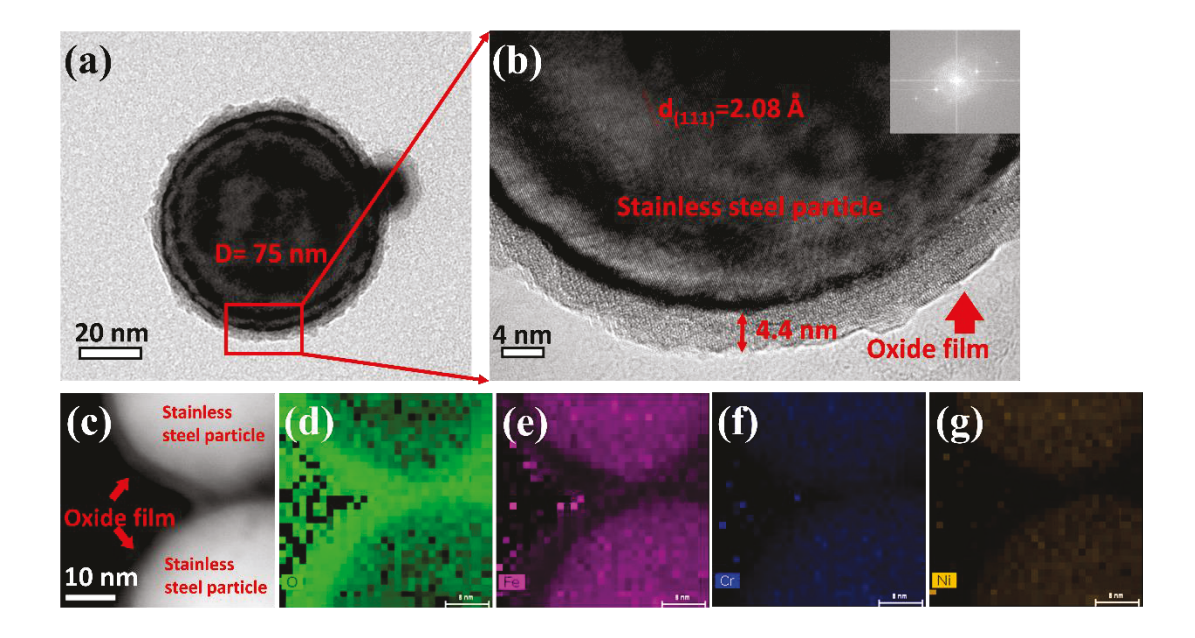


Figure 3. (a) TEM image of an SS316L nanoparticle. D= diameter. (b) High-resolution TEM image showing an ultra-thin oxide film (4-5 nm thick) on the surface of SS316L nanoparticle. (c) HAADF image of an interface between a SS316L nanoparticle with (d)-(g) the corresponding EDS mapping of O, Fe, Cr, and Ni elements, respectively.

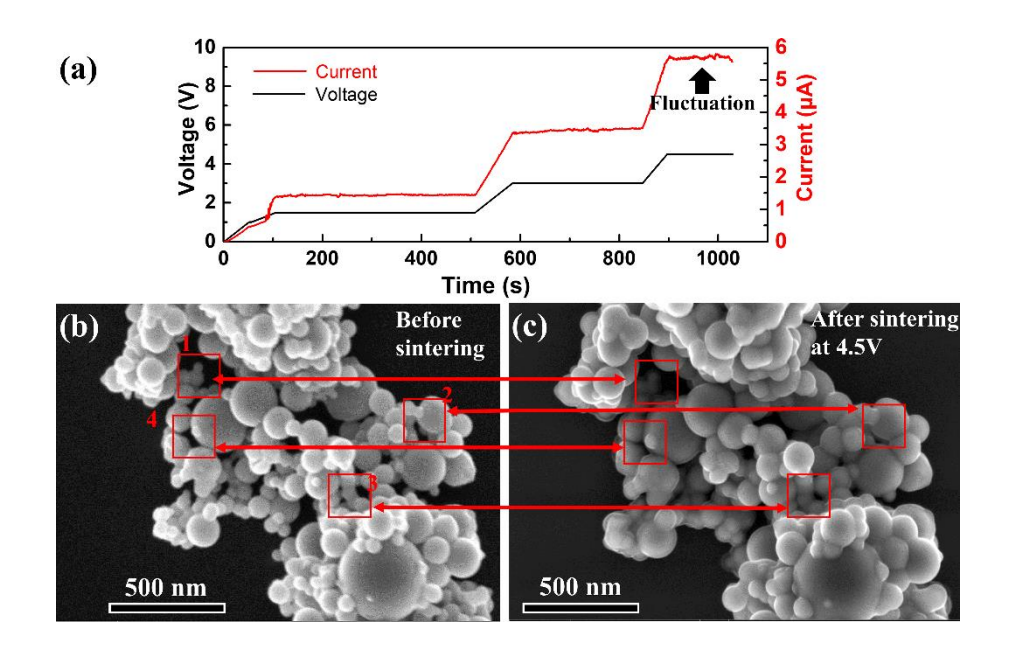


Figure 4. (a) The measured electrical current as a function of time with the stepwise increase of the applied electrical voltage to 4.5V. SEM images of the SS316L particles (b) before and (c) after the initial sintering at 4.5V.

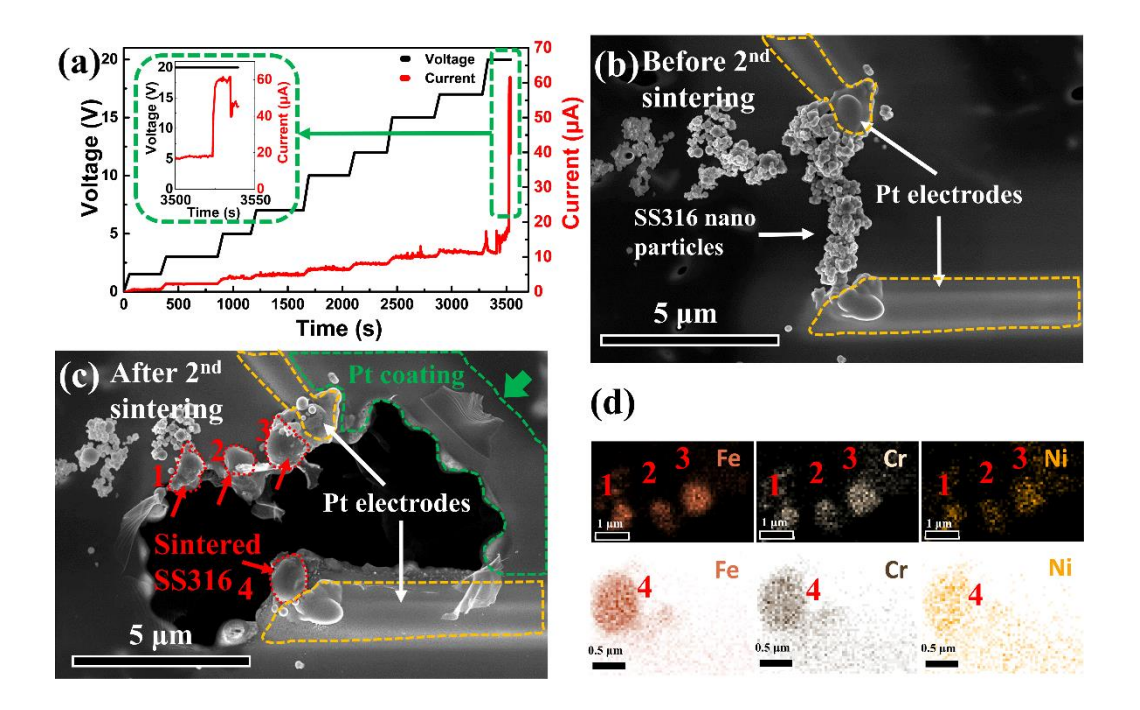


Figure 5. (a) The measured electrical current as a function of time with the stepwise increase of the applied electrical voltage to 20V. Insert: the enlarged view of the sudden changes of electrical current near 20 V. SEM image of SS316L nanoparticles (b) before and (c) and after the second sintering at 20V. The group of SS316L nanoparticles was connected to Pt electrodes. (d) EDS mapping of the distribution of the Fe, Cr, and Ni elements after the second sintering at 20V.

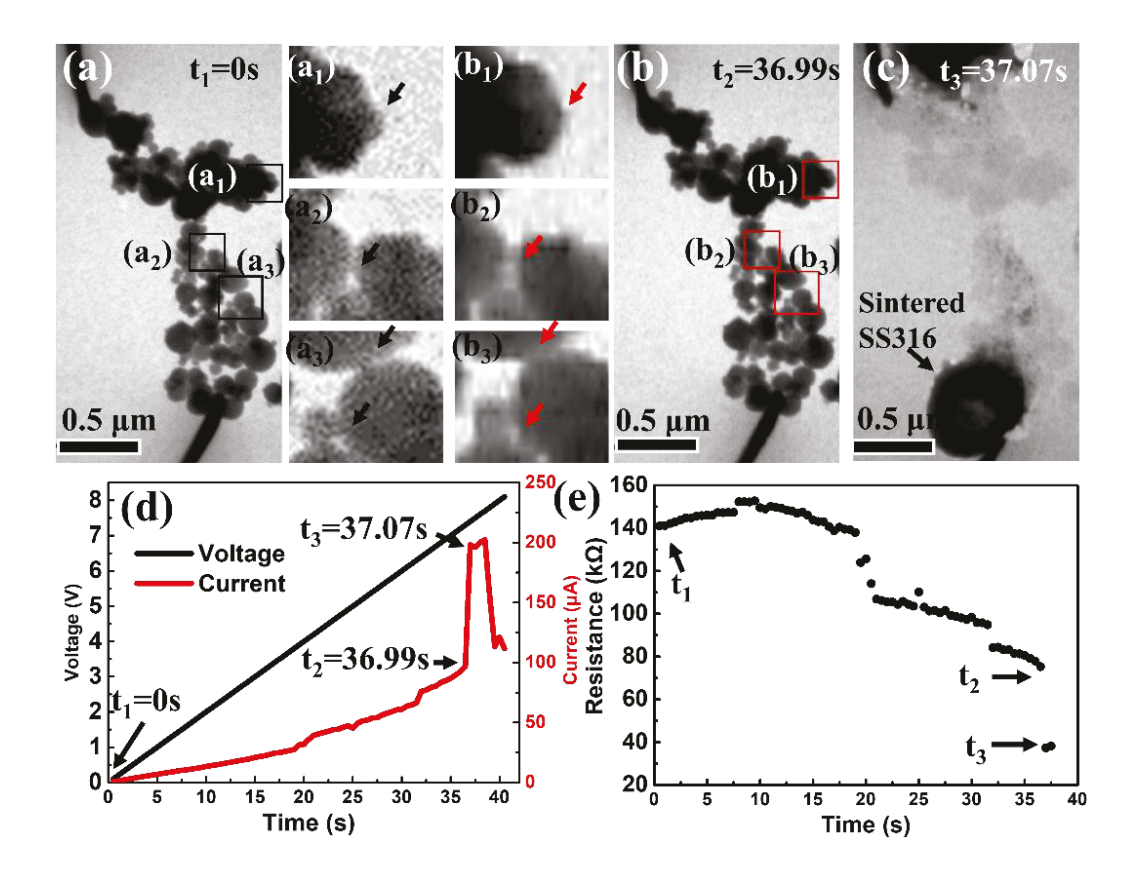


Figure 6. Bright-field TEM images of SS316L nanoparticles of (a) before sintering; (b) at t_1 =36.99 seconds (corresponding to 7.4 V); and (c) at t_2 =37.07 seconds. The features of microstructural changes are compared between (a_i) and (b_i), i=1, 2, 3. (d) The measured electrical current as a function of time with the linear increase of the applied electrical voltage at a constant rate of 0.2 V/s. (e) Evolution of electrical resistance as a function of time.

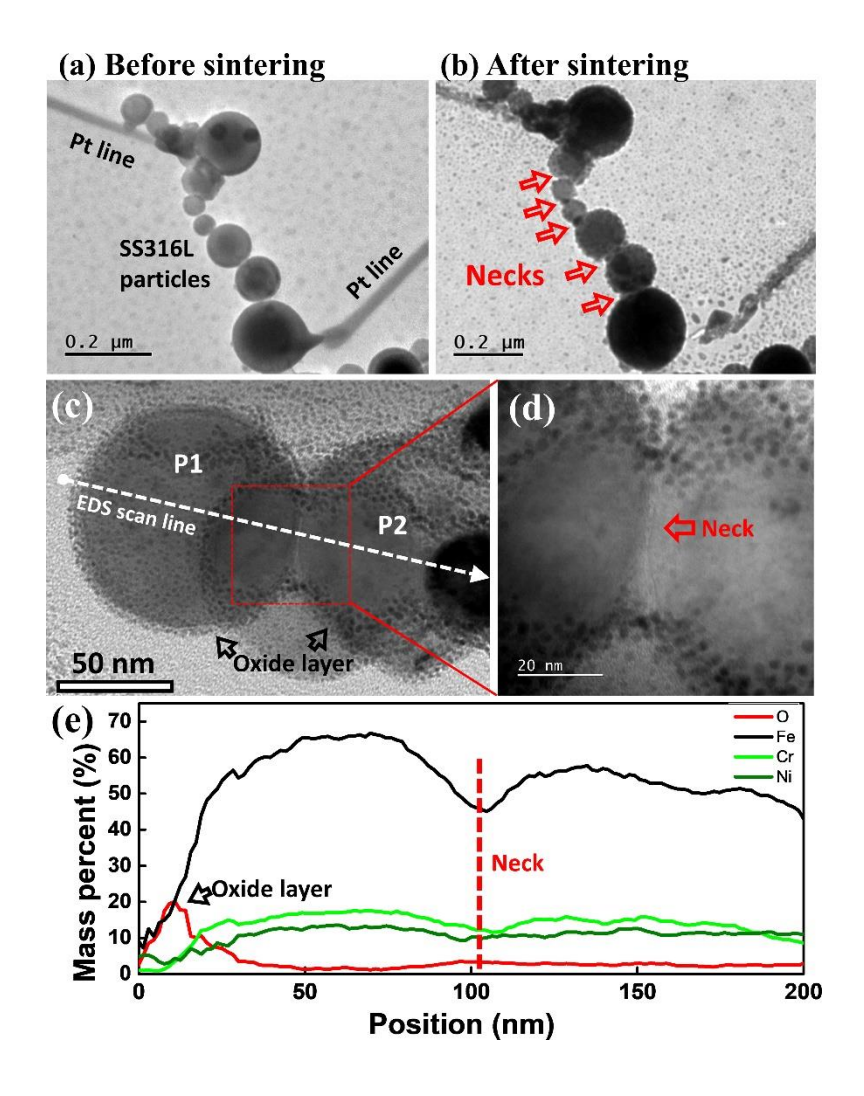


Figure 7. (a, b) TEM images showing the formation of necks between SS316L particles after EFAS. (c) Cross-section view of two particles (P1 and P2) after sintering; (d) an enlarged view of the interface between the two particles; (e) EDS line scan profiles of O, Fe, Cr and Ni elements distribution along the white dotted line in

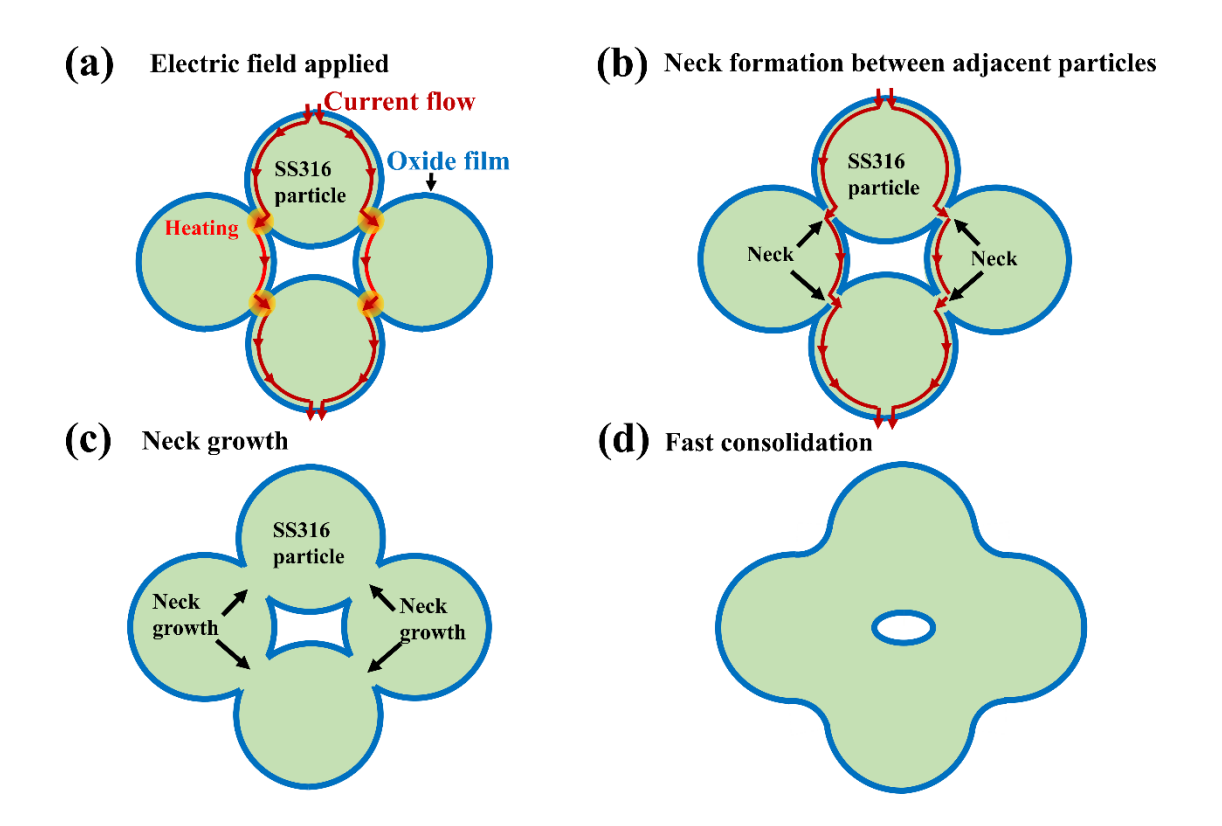


Figure 8. Schematic illustration of the four stages of the EFAC process of SS 316L nanoparticles: (a) cleaning of oxide film on the surface of nanoparticles by electric currents; (b) neck formation between the adjacent SS 316L nanoparticles; (c) neck growth between SS 316L nanoparticles; and (d) fast consolidation.